Science
AAAS

Increased Silver Activity for Direct Propylene Epoxidation via Subnanometer Size Effects

Y. Lei, *et al.*

Science **328**, 224 (2010);
DOI: 10.1126/science.1185200

positions of the five atoms as a function of time from one of the MD trajectories, bending the OCO angle from 180° to 175°, and calculating the dipole moments of $IBr^-(CO_2)$, as well as the sums of the dipole moments of the $IBr^- + CO_2$ and $I^-(CO_2)$ + Br fragments, calculated at their geometries in the complex. The differences between these quantities are shown in Fig. 4. After 200 fs, the presence of the CO_2 molecule leads to a shift of the excess charge away from the iodine atom and toward the bromine atom in the complex, compared to the charge distribution in IBr^-. This shift in the charge distribution reflects both charge transfer to the bromine due to the presence of the CO_2 molecule and charge delocalization between I^- and CO_2 in the $I^-(CO_2)$ complex. Based on these results, we conclude that, for times between 200 and 500 fs, the charge distribution of $IBr^-(CO_2)$ is perturbed relative to both asymptotes with greater negative charge on the Br atom. This time range corresponds well to the time at which the $I + Br^- + CO_2$ product channel is observed in the experiment and suggests that, at the time of the charge hop, the MD simulations underestimate the coupling between the adiabatic potential curves.

Taken together, the results of the calculations lead us to a mechanism for long-range electron transfer between I and Br in the dissociation of $IBr^-(CO_2)$ on the A′ electronic state. When the $I^-\cdots CO_2$ vibration reaches its first inner turning point (typically near a time delay of ~350 fs), the energy gap between the A′ and X or A states is minimized. A small number of trajectories sample regions of the potential where the gap between the A′ and A states is ~0.01 eV, and many of the trajectories have an energy gap that is commensurate with one or two quanta of CO_2 bending vibration. At these small values of R_{IC}, the CO_2 molecule will be bent, and the distorted OCO angle projects favorably onto the bend-excited states after the charge transfer. At the same time, the changes in the dipole moment along the IBr axis indicate that the presence of the CO_2 molecule shifts the excess charge density toward the bromine atom, thereby providing a mechanism for the increased coupling between the A′ and X or A electronic states. The mechanism and time scales are consistent with the observed Br^- products at ~350 fs in the TRPES experiment. It is likely that the intimate, essential involvement of solvent internal degrees of freedom, elucidated in this simple example of long-range electron transfer, will be a major component in other electron-transfer processes taking place through solvent bridges.

References and Notes

1. D. C. Clary, *Proc. Natl. Acad. Sci. U.S.A.* **105**, 12649 (2008).
2. D. M. Neumark, *Science* **272**, 1446 (1996).
3. J. C. Polanyi, A. H. Zewail, *Acc. Chem. Res.* **28**, 119 (1995).
4. G. C. Schatz, *Science* **262**, 1828 (1993).
5. K. M. Ervin, W. C. Lineberger, in *Advances in Gas Phase Ion Chemistry*, N. G. Adams, L. M. Babcock, Eds. (JAI Press, Greenwich, CT, 1992), vol. 1, pp. 121–66.
6. D. M. Neumark, *J. Chem. Phys.* **125**, 132303 (2006).
7. D. E. Manolopoulos *et al*., *Science* **262**, 1852 (1993).
8. P. G. Wenthold, D. A. Hrovat, W. T. Borden, W. C. Lineberger, *Science* **272**, 1456 (1996).
9. A. H. Zewail, *Angew. Chem. Int. Ed.* **39**, 2586 (2000).
10. V. Blanchet, M. Z. Zgierski, T. Seideman, A. Stolow, *Nature* **401**, 52 (1999).
11. O. Gessner *et al*., *Science* **311**, 219 (2006); published online 15 December 2005 (10.1126/science.1120779).
12. A. Stolow, A. E. Bragg, D. M. Neumark, *Chem. Rev.* **104**, 1719 (2004).
13. A. Sanov, W. C. Lineberger, *Phys. Chem. Chem. Phys.* **6**, 2018 (2004).
14. B. J. Greenblatt, M. T. Zanni, D. M. Neumark, *Science* **276**, 1675 (1997).
15. J. M. Papanikolas *et al*., *J. Chem. Phys.* **99**, 8733 (1993).
16. A. V. Davis, R. Wester, A. E. Bragg, D. M. Neumark, *J. Chem. Phys.* **117**, 4282 (2002).
17. A. V. Davis, M. T. Zanni, C. Frischkorn, D. M. Neumark, *J. Electron Spectrosc. Relat. Phenom.* **108**, 203 (2000).
18. D. H. Paik, N. J. Kim, A. H. Zewail, *J. Chem. Phys.* **118**, 6923 (2003).
19. D. E. Szpunar, K. E. Kautzman, A. E. Faulhaber, D. M. Neumark, *J. Chem. Phys.* **124**, 054318 (2006).
20. R. A. Relph *et al*., *Science* **327**, 308 (2010).
21. A. E. Bragg, M. C. Cavanagh, B. J. Schwartz, *Science* **321**, 1817 (2008).
22. M. A. Thompson, J. P. Martin, J. P. Darr, W. C. Lineberger, R. Parson, *J. Chem. Phys.* **129**, 224304 (2008).
23. R. Mabbs, K. Pichugin, A. Sanov, *J. Chem. Phys.* **122**, 174305 (2005).
24. P. Wernet *et al*., *Phys. Rev. Lett.* **103**, 013001 (2009).
25. T. Sanford, S. Y. Han, M. A. Thompson, R. Parson, W. C. Lineberger, *J. Chem. Phys.* **122**, 054307 (2005).
26. Experimental and theoretical methods are available as supporting material on *Science* Online.
27. D. W. Arnold, S. E. Bradforth, E. H. Kim, D. M. Neumark, *J. Chem. Phys.* **102**, 3510 (1995).
28. Y. X. Zhao, C. C. Arnold, D. M. Neumark, *J. Chem. Soc. Faraday Trans.* **89**, 1449 (1993).
29. M. Thompson, thesis, University of Colorado (2007).
30. H.-J. Werner *et al*., MOLPRO, version 2008.1, a package of ab initio programs, 2008 (www.molpro.net).
31. D. W. Arnold, S. E. Bradforth, E. H. Kim, D. M. Neumark, *J. Chem. Phys.* **97**, 9468 (1992).

32. We thank the NSF (W.C.L. and A.B.M.), the Air Force Office of Scientific Research (W.C.L.), and the Office of Naval Research (A.B.M.) for support of this work, as well as the Graduate School at The Ohio State University for fellowship support (S.H.). The calculations were performed on the JILA Yotta cluster and on the Glenn Cluster at the Ohio Supercomputer Center. S.H. is grateful to K. A. Peterson for his assistance with the electronic structure calculations.

Supporting Online Material

www.sciencemag.org/cgi/content/full/science.1184616/DC1
Materials and Methods
Figs. S1 to S9
Tables S1 and S2
References
Movies S1 to S3

12 November 2009; accepted 12 February 2010
Published online 4 March 2010;
10.1126/science.1184616
Include this information when citing this paper.

Increased Silver Activity for Direct Propylene Epoxidation via Subnanometer Size Effects

Y. Lei,[1,2]* F. Mehmood,[3]* S. Lee,[1]* J. Greeley,[4] B. Lee,[5] S. Seifert,[5] R. E. Winans,[5] J. W. Elam,[6] R. J. Meyer,[2] P. C. Redfern,[1] D. Teschner,[7] R. Schlögl,[7] M. J. Pellin,[3] L. A. Curtiss,[1,3,4]† S. Vajda[1,4,8]†

Production of the industrial chemical propylene oxide is energy-intensive and environmentally unfriendly. Catalysts based on bulk silver surfaces with direct propylene epoxidation by molecular oxygen have not resolved these problems because of substantial formation of carbon dioxide. We found that unpromoted, size-selected Ag_3 clusters and ~3.5-nanometer Ag nanoparticles on alumina supports can catalyze this reaction with only a negligible amount of carbon dioxide formation and with high activity at low temperatures. Density functional calculations show that, relative to extended silver surfaces, oxidized silver trimers are more active and selective for epoxidation because of the open-shell nature of their electronic structure. The results suggest that new architectures based on ultrasmall silver particles may provide highly efficient catalysts for propylene epoxidation.

Propylene oxide is a key precursor for the production of commodity chemicals. The current methods that can produce propylene oxide on an industrial scale are either not profitable or are environmentally unfriendly because of the production of chlorinated or peroxycarboxylic waste (*1*). Thus, direct partial oxidation of propylene by molecular oxygen, as shown in Scheme 1, has received considerable attention (*2*–*8*). However, no industrial-scale heterogeneous catalytic propylene epoxidation process using molecular oxygen has yet been identified. Silver has been successfully used in the epoxidation of ethylene with high selectivity, both in the lab (*6*) and on an industrial scale (*9*). However, the use of silver in propylene ep-

[1]Chemical Sciences and Engineering Division, Argonne National Laboratory, Argonne, IL 60439, USA. [2]Department of Chemical Engineering, University of Illinois, Chicago, IL 60607, USA. [3]Materials Science Division, Argonne National Laboratory, Argonne, IL 60439, USA. [4]Center for Nanoscale Materials, Argonne National Laboratory, Argonne, IL 60439, USA. [5]X-ray Sciences Division, Argonne National Laboratory, Argonne, IL 60439, USA. [6]Energy Systems Division, Argonne National Laboratory, Argonne, IL 60439, USA. [7]Department of Inorganic Chemistry, Fritz-Haber-Institut der Max-Planck-Gesellschaft, Faradayweg 4-6, 14195 Berlin, Germany. [8]Department of Chemical Engineering, Yale University, New Haven, CT 06520, USA.

*These authors contributed equally to this work.
†To whom correspondence should be addressed. E-mail: curtiss@anl.gov (L.A.C.); vajda@anl.gov (S.V.)

oxidation has been hampered by either low conversion or poor selectivity toward propylene oxide, and the detailed mechanism of the epoxidation process is unclear (*2*, *5*, *7*, *8*, *10*).

The catalytic activity of metals can be altered when used as small metal clusters or nanoparticles (*11*–*15*), and epoxidation of propylene to propylene oxide on silver and gold nanoparticle catalysts exhibits strongly size-dependent catalytic activity (*2*, *4*, *5*, *16*). However, none of the nanocatalysts reported to date possess both high conversion and selectivity toward propylene oxide. Haruta and co-workers discovered a highly selective propene epoxidation catalyst based on titania-supported gold nanoparticles (2 to 4 nm in diameter) when hydrogen was co-fed with the oxygen and propylene mixture (*4*), but the selectivity was extremely sensitive to the gold nanoparticle size and shape. Size-preselected subnanometer gold clusters stabilized on amorphous alumina have highly selective catalysts for this reaction (*17*), and supported subnanometer Pt clusters are both highly active and selective for oxidative propane dehydrogenation (*18*).

A report that gas-phase anionic silver clusters exhibit activity in oxidation reactions at very low temperatures (*19*) led us to investigate the catalytic properties of supported silver trimers and to use quantum chemical calculations to help explain the unprecedented activity and selectivity observed for propylene epoxidation on them. In addition to size-selected silver trimers (Ag_3) supported on amorphous alumina films, we have also investigated the catalytic properties of very small nanoparticles with average size of ~3.5 nm (2 nm in height and 4 nm in diameter) resulting from agglomeration of the silver trimers at higher temperatures. The silver cluster–based catalysts were fabricated by depositing mass-selected clusters from a molecular beam on an ultrathin alumina film (~3 monolayers) produced by atomic layer deposition on top of the naturally oxidized silicon wafer (*20*). The cluster deposition apparatus has been described in detail elsewhere (*21*). Briefly, a narrow size distribution of Ag_n^+ ($n = 2$ to 4) clusters with dominant trimer contribution was mass-selected using a quadrupole mass filter and deflector assembly and deposited on the support at 2.2% atomic monolayer coverage.

$$2CH_3\text{-}CH{=}CH_2 + O_2 \xrightarrow{\text{Catalyst}} 2$$

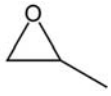

Scheme 1.

A common problem encountered with the use of small metal particles on oxide supports is that their catalytic performance is often diminished by sintering, the agglomeration of particles caused by heating during reactions (*22*, *23*). In situ grazing incidence small-angle x-ray scattering (GISAXS) is a powerful tool to study the evolution of size and shape of supported clusters and nanoparticles under reaction conditions (*24*). GISAXS revealed that the sintering of Ag_3 clusters begins around 110°C, leading to the formation of silver particles with average size of 3.5 nm at 200°C (Fig. 1A). The analysis of the two-dimensional GISAXS data revealed particle height and diameter of 2 nm and 4 nm, respectively. These nanoparticles did not sinter further during an additional 1 hour of monitoring of the reaction. There was no evidence of any sintering of the trimers before the abrupt change at 110°C (*25*), which is consistent with the results of Buratto *et al*. (*26*), who found silver trimers to be stable on a titania surface. Because the silver trimers remain isolated only below 110°C, their catalytic properties are discussed for this temperature region.

Catalytic tests on the silver trimer and nanoparticles were performed using temperature-programmed reaction at 133 kPa and gas flow of 30 sccm (standard cubic centimeters per minute). The composition of the gas mixture was 0.67% C_3H_6 and 0.33% O_2 in helium. The reaction products were analyzed on a differentially pumped quadrupole mass spectrometer. Propylene oxide, acrolein, and carbon dioxide were identified as the dominant reaction products from the silver trimers (Fig. 1B; note that for the silver trimer, the number of surface atoms equals the number of total atoms of the cluster). The formation of acetone and propenol was excluded on the basis of analysis of the mass spectra (*25*). Beginning at room temperature, the rate of both propylene oxide and acrolein formation increased sharply with temperature. At 60°C we observed the onset of combustion. The formation of CO_2 coincided with the decrease of acrolein production, which indicates that these two channels are competitive. Figure 1C shows two regions for product selectivity below the sintering temperature. At temperatures up to 60°C, the selectivity was highest for acrolein; between 70°C and 100°C, much higher propylene oxide/acrolein product ratios (3:1) were achieved. However, this improvement is realized at the expense of an increase in CO_2 formation of 30 to 60%.

The catalytic performance of the nanoparticle aggregates was strikingly different from the performance of their subnanometer Ag_3 counterparts under identical reaction conditions (Fig. 2). The nanoparticles exhibited superior selectivity toward propylene oxide at temperatures up to 120°C while maintaining activity per surface atom comparable to that of Ag_3 clusters. Combustion on the nanosized aggregates had an onset at 130°C, a temperature 70°C higher than on Ag_3. The rate of propylene oxide molecules formed per surface silver atom was ~1 s^{-1} at 110°C for both Ag_3 and the silver aggregates, which is much greater than that reported for any silver catalyst. For example, turnover rates per surface atom (an estimated $\leq 10^{-4}$ per total atom) were reported to be 10^{-2} s^{-1} for 50- to 660-nm unpromoted silver particles at much higher temperatures [220°C (*2*)] and ~5 × 10^{-3} s^{-1} for an Ag-Ni catalyst (3:1 weight ratio)

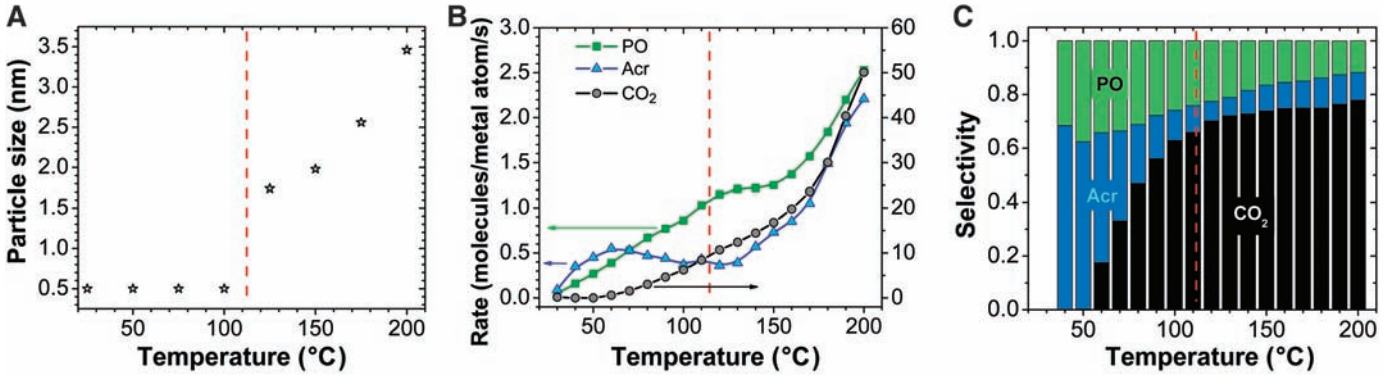

Fig. 1. (**A**) Temperature-dependent average cluster size from GISAXS. (**B**) Rate of propylene oxidation toward propylene oxide (PO), acrolein (Acr), and CO_2 per surface silver atom. (**C**) Selectivity of propylene oxide, acrolein, and CO_2 versus temperature. The vertical dashed lines indicate the temperature at which the sintering of the silver trimers begins. During an additional hour of reaction at 200°C, no change in the size of the aggregates was observed and the turnover rate for propylene oxide decreased to 1.55 s^{-1}, which likely indicates annealing of the newly formed nanostructure. The data shown are results from one run. The estimated uncertainty of GISAXS is ~ ±0.2 nm and ~5% for the turnover rates (*25*).

tested in the 150° to 300°C temperature range (*27*). Thus, the observed turnover rates in this work are orders of magnitude higher than the previously reported data (*25*). With respect to other subnanometer catalysts, the turnover rate of Ag_3 is greater by a factor of 4 than that obtained for $Au_{6\text{-}10}$ under identical reaction conditions with comparable selectivity toward propylene oxide (*17*). Also, x-ray photoemission spectroscopy (XPS) analysis of carbon coverage yielded no evidence of degradation of the catalytic activity of the aggregates over 4 hours, nor any evidence of deactivation by carbon.

The electronic structure of small clusters and nanoparticles can control catalytic activity (*28*, *29*). We carried out an ultrahigh-vacuum x-ray photoemission (UHV XPS) experiment on the Ag_3 clusters and in situ XPS on the Ag nanoparticles in the presence of the reactants and under reaction conditions (*25*) to determine the oxidation state of silver. The Ag_3 clusters show a typical positive shift and broadening of the Ag 3d core level characteristic for small supported clusters (*29*, *30*). The 3d (5/2) core level was observed at ~368.6 eV when the energy scale was aligned according to the Si 2p (3/2) metallic core level of the substrate at 99.2 eV. The observed shift of the Ag 3d core level of the Ag_3 clusters is 0.2 to 0.4 eV less than that reported for small silver clusters of similar size (*31*, *32*), which indicates that the silver trimers are partially oxidized. (If silver is oxidized, Ag 3d is negatively shifted, as opposed to the core levels of almost all other elements.) This observation is confirmed by the results of theoretical calculations, which show increased positive charge on Ag_3 with an oxygen atom adsorbed (*25*).

An in situ XPS measurement performed on Ag particles 2 nm in height and 4 nm in diameter (*25*) showed that even these particles exhibited broadening and positive shifts in the Ag 3d spectrum relative to the metallic reference. Considering the magnitude of the shift and the size of these particles, as well as the fact that the spectrum can be described with one Gauss-Lorenz curve, it is likely that the silver nanoparticles are mostly metallic during propylene oxidation, with any oxidized contribution below 5%.

We carried out periodic, self-consistent density functional (PW91) calculations to understand the observation that Ag_3 clusters on an alumina support catalyze propylene epoxidation with only a negligible amount of carbon dioxide and high activity at low temperatures. Previous computational work on this reaction has focused exclusively on idealized single-crystal Ag surfaces (*33*). Torres *et al.* have reported a density functional theory (DFT) study of propylene epoxidation on an Ag(111) surface (*34*). They investigated two reaction pathways: (i) oxygen transfer from the silver surface to the propylene via an oxametallacycle intermediate for the formation of propylene oxide, and (ii) hydrogen abstraction from propylene by surface oxygen to form an allyl radical that is postulated to lead to

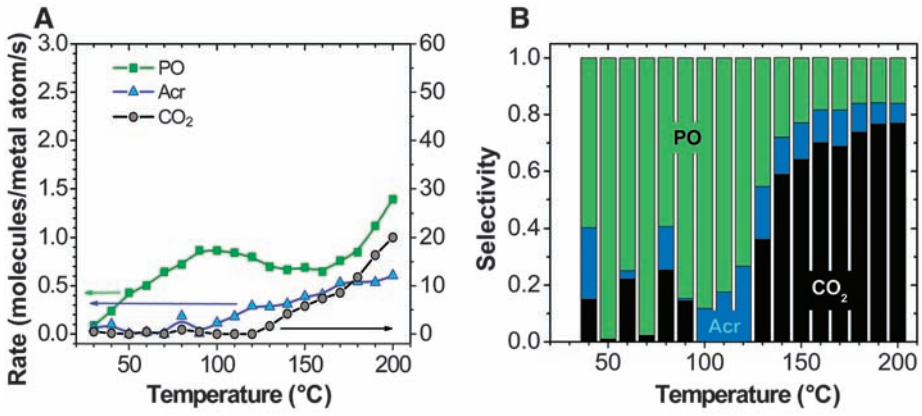

Fig. 2. (**A** and **B**) Rate of propylene oxidation toward propylene oxide, acrolein, and CO_2 per surface silver atom (A) and selectivity (B) on the nanometer-sized, sintering-resistant silver aggregates that formed from Ag_3 clusters during the first reaction cycle. The turnover rate of 1.4 s^{-1} for propylene oxide at 200°C is in agreement with the activity data obtained after annealing of the sample at 200°C. This finding and the comparable selectivities observed at 200°C (compare Fig. 1C with Fig. 2B) indicate a high stability of the ~3.5-nm catalyst during 4 hours of reaction.

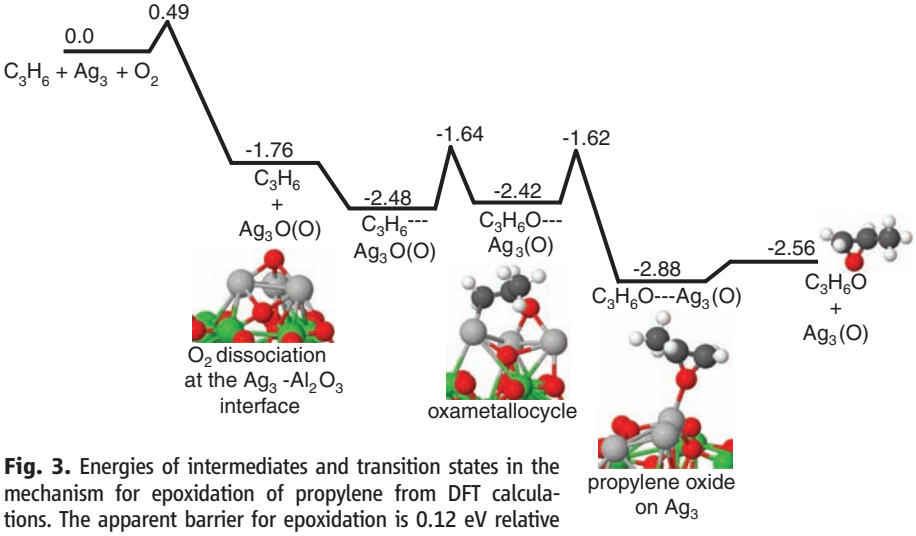

Fig. 3. Energies of intermediates and transition states in the mechanism for epoxidation of propylene from DFT calculations. The apparent barrier for epoxidation is 0.12 eV relative to gas-phase propylene and Ag_3 with dissociated O_2. There are two different oxygen sites resulting from dissociation of O_2 at the trimer-alumina surface interface: (i) the three-fold site on Ag_3, and (ii) alumina at the interface with Ag_3. The latter oxygen is indicated in parentheses. The reaction pathway as shown will result in excess interface oxygen, which can be removed either by migration to the three-fold site (calculated barrier of ~1 eV) or by diffusion and recombination on the alumina surface [diffusion on the surface should be possible according to (*37*)].

combustion products. The latter pathway had a lower barrier, which is consistent with combustion being favored over epoxidation on Ag(111). In contrast, combustion products are not as favorable in ethylene epoxidation on a silver surface because it is not possible to form an allyl-like species from ethylene (*35*). The high activity and small amount of combustion products at low temperatures observed for Ag_3 suggest that the reaction mechanism is different from that at the Ag(111) surface, and this was confirmed by our DFT calculations.

Reaction pathways for propylene epoxidation and acrolein formation were investigated; the results, including some key intermediate structures, are summarized in Figs. 3 and 4. An Ag_3 cluster adsorbed on a (010) θ alumina surface was used as a model for the catalytic reaction site. Our calculations indicate that dissociation of the oxygen molecule occurs at the interface of Ag_3 and the alumina surface with a barrier of 0.49 eV. This result suggests that two types of oxygen atoms are present at Ag_3 sites (Figs. 3 and 4): one at the interface of Ag_3 and the alumina surface, and the other in the three-fold site on Ag_3. The barrier for O_2 dissociation at the interface is much lower than the barrier of 1.19 eV on an Ag(111) surface for 0.33 monolayer of O_2. In the analysis that follows, given the low dissociation barrier and strong oxygen binding, we assume that dissociative O_2 adsorption is equilibrated and that the two types of sites available to oxygen atoms are occupied at high coverage.

The energetics of the proposed epoxidation mechanism from the DFT calculations are

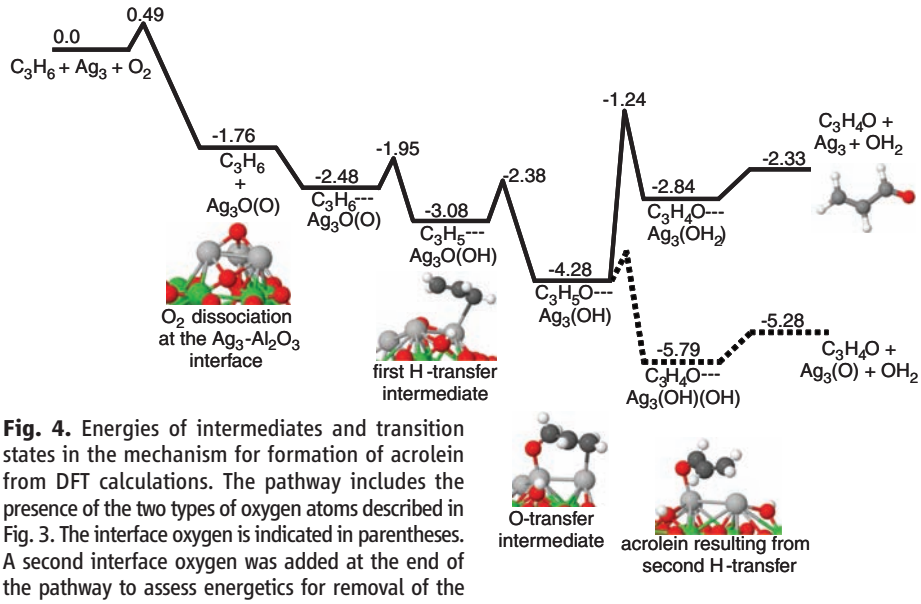

Fig. 4. Energies of intermediates and transition states in the mechanism for formation of acrolein from DFT calculations. The pathway includes the presence of the two types of oxygen atoms described in Fig. 3. The interface oxygen is indicated in parentheses. A second interface oxygen was added at the end of the pathway to assess energetics for removal of the second hydrogen. The required starting $Ag_3O(O)(O)$ configuration for this can be formed by O_2 dissociation on the $Ag_3(O)$ resulting from propylene epoxidation. Because acrolein formation involves removal of both types of oxygen atoms, it will be a closed catalytic cycle.

summarized in Fig. 3. After O_2 dissociation at the Ag_3-alumina interface, the first step involves oxygen transfer from the three-fold site to propylene to form an oxametallacyle (Fig. 3). This reaction has an apparent barrier of 0.12 eV relative to gas-phase propylene and Ag_3 with dissociated O_2 (this is the appropriate reference state for the effective barrier for epoxidation, assuming that propylene adsorption is weakly transient and does not compete directly with oxygen for adsorption sites). The second step involves oxygen addition to the double bond and is exothermic. Reaction pathways occurring from the oxametallacycle intermediate leading to the formation of other products such as acrolein, carbon dioxide, and propanal were investigated and found to be unfavorable. The apparent barrier for the first step of 0.12 eV is in good agreement with the experimental estimate for propylene oxide formation of 0.27 ± 0.1 eV (*25*).

An alternative pathway based on hydrogen abstraction from propylene leads to acrolein formation (Fig. 4). The first step involves hydrogen abstraction by the interface oxygen from the methyl group to form an allyl-like intermediate and an OH group. No barrier for this reaction is found relative to the gas-phase propylene and Ag_3 with dissociated O_2, in agreement with our experimental results (*25*). The second step involves oxygen addition to the allyl-like intermediate and is again exothermic. Formation of acrolein requires abstraction of a second hydrogen, and the DFT calculations indicate that it is highly unfavorable to transfer this additional hydrogen atom to the existing interfacial OH group (resulting in water formation). In contrast, abstraction by a second interfacial oxygen (formed during a previous catalytic cycle) to form an OH group is thermodynamically favorable. The acrolein pathway is also likely to result in combustion products, as it is usually assumed that allyl-like intermediates can initiate combustion (*34*). Further evidence for this hypothesis comes from the experimental observation that combustion and acrolein formation occur in the same reaction channel.

Our DFT investigation can account for the surprisingly high catalytic activity and selectivity found for the silver trimers. The calculations indicate that an alumina-supported Ag_3O cluster has a substantial net spin density (~0.6) on the Ag and O in the cluster. In contrast, there is no spin density present when atomic oxygen is adsorbed on an Ag(111) surface, assuming low oxygen coverage. Such a surface has a barrier to oxametallacycle formation of ~0.7 eV from our calculations and those of Torres *et al.* (*34*), which compares to 0.12 eV for the trimer. In addition, we calculated the spin density on an alumina-supported closed-shell Ag_4O cluster and found it to be zero. The barrier to formation of an oxametallacycle structure was calculated on a gas-phase Ag_4O cluster and is much higher (0.5 eV) than that of the trimer. Thus, the results for both the Ag(111) surface and the Ag_4 cluster suggest that the partially filled s-d hybridized energy level of the supported oxidized Ag_3 cluster gives it an open-shell electronic structure character, which makes it highly reactive toward the propylene double bond. This result is consistent with the observed higher activity for propylene oxide formation and the small amount of CO_2 produced at low temperatures (because CO_2 formation is initiated by C-H bond activation rather than by oxygen attack). The experimental barrier for CO_2 formation is much greater at 0.7 ± 0.2 eV (*25*), which is consistent with the calculated O_2 dissociation barrier of 0.5 eV and suggests that combustion of propylene, which requires more oxygen and involves strongly interacting propylene fragment intermediates that can impede O_2 dissociation, has O_2 dissociation as its rate-limiting step. The high activity of the 2 nm × 4 nm nanoparticles, which is the same per surface atom as the Ag_3 clusters, may also be due to electronic effects involving surface spin density sites similar to Ag_3, or possibly some other electronic structure feature. The surfaces of the nanoparticles resulting from agglomeration of the trimers are likely to have disordered structures, as extrapolated from scanning tunneling microscopy and molecular dynamics studies (*36*) of Ag nanoparticles with shapes and sizes similar to those we observed. Density functional calculations (*25*) indicate that Ag nanoclusters with structural disorder have isomers very close in energy, including some in high spin states; therefore, propylene epoxidation may be catalyzed by surface spin density on the agglomerated nanoparticles.

In the case of acrolein formation, the oxygen at the interface of the Ag_3 cluster is highly reactive for hydrogen abstraction from propylene, with no barrier for the first hydrogen abstraction step from DFT calculations. This can account for the high activity observed for acrolein formation on the silver trimer and the small amount of CO_2 produced at low temperatures. The much smaller amount of acrolein produced on the nanoparticles is consistent with an acrolein reaction mechanism based on hydrogen abstraction by the interfacial oxygen, as opposed to the oxygen adsorbed on a three-fold site; the amount of interfacial oxygen will be much smaller for the nanoparticles than for the Ag trimers. The smaller fraction of nanoparticle-alumina interfacial sites for O_2 dissociation may also explain why the combustion products desorb at a higher temperature on the nanoparticles than on the Ag trimers. The proposed acrolein reaction mechanism suggests that addition of H_2O to the feed stream could reduce the acrolein production and enhance propylene epoxidation formation, because water is a product on this pathway (Fig. 4). This expectation is in accord with the pronounced effect of water in increasing the selectivity toward propylene oxide formation observed in the case of Au_{6-10} clusters (*17*).

References and Notes

1. K. Weissermel, H.-J. Arpe, *Industrial Organic Chemistry* (Wiley-VCH, Weinheim, Germany, ed. 4, 2003).
2. J. Lu, J. J. Bravo-Suárez, A. Takahashi, M. Haruta, S. T. Oyama, *J. Catal.* **232**, 85 (2005).
3. T. A. R. Nijhuis, T. Visser, B. M. Weckhuysen, *Angew. Chem. Int. Ed.* **44**, 1115 (2005).
4. T. Hayashi, K. Tanaka, M. Haruta, *J. Catal.* **178**, 566 (1998).
5. F. W. Zemichael, A. Palermo, M. S. Tikhov, R. M. Lambert, *Catal. Lett.* **80**, 93 (2002).
6. R. M. Lambert, F. J. Williams, R. L. Cropley, A. Palermo, *J. Mol. Catal. Chem.* **228**, 27 (2005).
7. M. F. Luo, J. Q. Lu, C. Li, *Catal. Lett.* **86**, 43 (2003).
8. W. Yao *et al.*, *Catal. Lett.* **119**, 185 (2007).
9. J. G. Serafin, A. C. Liu, S. R. Seyedmonir, *J. Mol. Catal. Chem.* **131**, 157 (1998).

10. M. A. Barteau, R. J. Madix, *J. Am. Chem. Soc.* **105**, 344 (1983).
11. Z. Xu *et al.*, *Nature* **372**, 346 (1994).
12. M. S. Chen, D. W. Goodman, *Science* **306**, 252 (2004); published online 26 August 2004 (10.1126/science.1102420).
13. C. Lemire, R. Meyer, S. Shaikhutdinov, H.-J. Freund, *Angew. Chem. Int. Ed.* **43**, 118 (2004).
14. A. T. Bell, *Science* **299**, 1688 (2003).
15. F. Tao *et al.*, *Science* **322**, 932 (2008); published online 9 October 2008 (10.1126/science.1164170).
16. A. L. de Oliveira, A. Wolf, F. Schuth, *Catal. Lett.* **73**, 157 (2001).
17. S. Lee *et al.*, *Angew. Chem. Int. Ed.* **48**, 1467 (2009).
18. S. Vajda *et al.*, *Nat. Mater.* **8**, 213 (2009).
19. L. D. Socaciu *et al.*, *J. Chem. Phys.* **120**, 2078 (2004).
20. J. W. Elam, Z. A. Sechrist, S. M. George, *Thin Solid Films* **414**, 43 (2002).
21. R. E. Winans *et al.*, *Top. Catal.* **39**, 145 (2006).
22. D. H. Kim, Y. H. Chin, J. H. Kwak, J. Szanyi, C. H. F. Peden, *Catal. Lett.* **105**, 259 (2005).
23. S. Wodiunig, J. M. Keel, T. S. E. Wilson, F. W. Zemichael, R. M. Lambert, *Catal. Lett.* **87**, 1 (2003).
24. S. Vajda *et al.*, *J. Chem. Phys.* **131**, 121104 (2009).
25. See supporting material on *Science* Online.
26. L. Benz *et al.*, *J. Chem. Phys.* **122**, 081102 (2005).
27. A. Takahashi, N. Hamakawa, I. Nakamura, T. Fujitani, *Appl. Catal. A* **294**, 34 (2005).
28. R. Dietsche *et al.*, *Appl. Phys. A* **90**, 395 (2008).
29. W. E. Kaden, T. Wu, W. A. Kunkel, S. L. Anderson, *Science* **326**, 826 (2009).
30. W. F. Egelhoff Jr., *Surf. Sci. Rep.* **6**, 253 (1987).
31. R. Dietsche, thesis, Univesität Konstanz (2009).
32. K. Luo *et al.*, *J. Phys. Chem. B* **109**, 4064 (2005).
33. M. C. Zonnevylle, R. Hoffmann, P. J. Vandenhoek, R. A. van Santen, *Surf. Sci.* **223**, 233 (1989).
34. D. Torres, N. Lopez, F. Illas, R. M. Lambert, *Angew. Chem. Int. Ed.* **46**, 2055 (2007).
35. S. Linic, M. A. Barteau, *J. Am. Chem. Soc.* **125**, 4034 (2003).
36. R. E. Palmer, S. Pratontep, H. G. Boyen, *Nat. Mater.* **2**, 443 (2003).
37. P. Gamallo, R. Sayós, *Phys. Chem. Chem. Phys.* **9**, 5112 (2007).
38. Work at Argonne National Laboratory was supported by the U.S. Department of Energy, Office of Basic Energy Sciences (Chemical Sciences, Materials Sciences, and Scientific User Facilities), under contract DE-AC-02-06CH11357. We thank the BESSY staff for their support. Also supported by the American Chemical Society Petroleum Research Fund (Y.L. and R.J.M.) and the U.S. Air Force Office of Scientific Research (S.V.). We acknowledge grants of computer time at the Molecular Science Computing Facility at Pacific Northwest National Laboratory and the Laboratory Computing Resource Center at Argonne National Laboratory. A Full Utility Patent Application was filed by Argonne in March 2009, entitled "Subnanometer and Nanometer Catalysts, Method for Preparing Size-Selected Catalyst" (Application 12/402,948).

Supporting Online Material

www.sciencemag.org/cgi/content/full/328/5975/224/DC1
Materials and Methods
Figs. S1 to S27
Tables S1 to S4
References

25 November 2009; accepted 24 February 2010
10.1126/science.1185200

Metabolic Syndrome and Altered Gut Microbiota in Mice Lacking Toll-Like Receptor 5

Matam Vijay-Kumar,[1] Jesse D. Aitken,[1] Frederic A. Carvalho,[1] Tyler C. Cullender,[2] Simon Mwangi,[3] Shanthi Srinivasan,[3] Shanthi V. Sitaraman,[3] Rob Knight,[4] Ruth E. Ley,[2] Andrew T. Gewirtz[1]*

Metabolic syndrome is a group of obesity-related metabolic abnormalities that increase an individual's risk of developing type 2 diabetes and cardiovascular disease. Here, we show that mice genetically deficient in Toll-like receptor 5 (TLR5), a component of the innate immune system that is expressed in the gut mucosa and that helps defend against infection, exhibit hyperphagia and develop hallmark features of metabolic syndrome, including hyperlipidemia, hypertension, insulin resistance, and increased adiposity. These metabolic changes correlated with changes in the composition of the gut microbiota, and transfer of the gut microbiota from TLR5-deficient mice to wild-type germ-free mice conferred many features of metabolic syndrome to the recipients. Food restriction prevented obesity, but not insulin resistance, in the TLR5-deficient mice. These results support the emerging view that the gut microbiota contributes to metabolic disease and suggest that malfunction of the innate immune system may promote the development of metabolic syndrome.

Humanity is facing an epidemic of interrelated metabolic diseases collectively referred to as metabolic syndrome, the hallmarks of which include hyperglycemia, hyperlipidemia, insulin resistance, obesity, and hepatic steatosis (*1*). The increasing incidence of metabolic syndrome is widely thought to result from nutrient excess due to increased food consumption and/or reduced levels of physical activity. Such nutrient excess results in obesity and may activate endoplasmic reticulum stress pathways resulting in chronic activation of proinflammatory kinase cascades that desensitize the metabolic response to insulin (*2*). Such insulin resistance can result in hyperglycemia and, in some cases, type 2 diabetes. Recent work suggests a possible role for the gut microbiota in obesity (*3*) and, consequently, other aspects of metabolic syndrome. In both humans and mice, the development of obesity correlates with shifts in the relative abundance of the two dominant bacterial phyla in the gut, the *Bacteroidetes* and the *Firmicutes* (*4*–*6*). In addition, it has been shown that transfer of the gut microbiota from obese (*ob/ob*) mice to germ-free wild-type (WT) recipients leads to an increase in fat mass in the recipients, leading to speculation that the gut microbiota promotes obesity by increasing the capacity of the host to extract energy (calories) from ingested food (*7*).

The gut microbiota is shaped by both environment and host genetics, with the innate immune system in particular, long appreciated for its role in defending against infection by pathogenic microbes, now suggested to play a key role in regulating the gut microbiota (*8*). Thus, in addition to its role in infection/inflammation, innate immunity may play a key role in promoting metabolic health. Toll-like receptor (TLR) 5 is a transmembrane protein that is highly expressed in the intestinal mucosa and that recognizes bacterial flagellin. In previous work with mice genetically deficient in TLR5 (T5KO mice), we found that 10% of the mutant mice exhibited severe colitis and an additional 30% exhibited gross and/or histopathologic evidence of colitis (*9*). The remaining 60% of the T5KO mice exhibited broadly elevated proinflammatory gene expression but lacked the histopathologic features that define colitis; however, we observed that, by 4 weeks of age, these mice had body masses that were on average 15% higher than those of their WT littermates. To eliminate potential opportunistic pathogens that may have been present in T5KO and WT littermates, and to make their gut microbiota similar to that of mice from the Jackson Laboratory (the world's largest supplier of research mice), we "rederived" T5KO mice by transplanting embryos into mice purchased from this supplier (*10*). Such standardization of the microbiota in the T5KO mice greatly attenuated the severity of their colitis and resulted in a more uniform phenotype characterized by mild inflammation (fig. S1) and obesity (Fig. 1).

Analysis of these rederived mice showed that, at 20 weeks of age, both male and female T5KO mice had body masses that were 20% greater than those of WT mice (Fig. 1A). Magnetic resonance imaging (MRI) revealed increased fat mass throughout the body of the T5KO mice, with a particular increase in visceral fat (Fig. 1B). T5KO mice had epididymal fat pads that were about twice as large as those in WT littermates at 20 weeks of age (Fig. 1, C and D). This increase

[1]Department of Pathology, Emory University, Atlanta, GA 30322, USA. [2]Department of Microbiology, Cornell University, Ithaca, NY 14853, USA. [3]Department of Medicine, Emory University, Atlanta, GA 30322, USA. [4]Howard Hughes Medical Institute, Department of Chemistry and Biochemistry, University of Colorado, Boulder, CO 80309, USA.

*To whom correspondence should be addressed. E-mail: agewirt@emory.edu